

AD_____

AWARD NUMBER: W81XWH-04-1-0042

TITLE: Transurethral Ultrasound Diffraction Tomography

PRINCIPAL INVESTIGATOR: Matthias C. Schabel, Ph.D.
Dilip Ghosh Roy, Ph.D.
Altaf Khan

CONTRACTING ORGANIZATION: University of Utah
Salt Lake City, Utah 84112-9351

REPORT DATE: March 2006

TYPE OF REPORT: Annual

PREPARED FOR: U.S. Army Medical Research and Materiel Command
Fort Detrick, Maryland 21702-5012

DISTRIBUTION STATEMENT: Approved for Public Release;
Distribution Unlimited

The views, opinions and/or findings contained in this report are those of the author(s) and should not be construed as an official Department of the Army position, policy or decision unless so designated by other documentation.

REPORT DOCUMENTATION PAGE

Form Approved
OMB No. 0704-0188

Public reporting burden for this collection of information is estimated to average 1 hour per response, including the time for reviewing instructions, searching existing data sources, gathering and maintaining the data needed, and completing and reviewing this collection of information. Send comments regarding this burden estimate or any other aspect of this collection of information, including suggestions for reducing this burden to Department of Defense, Washington Headquarters Services, Directorate for Information Operations and Reports (0704-0188), 1215 Jefferson Davis Highway, Suite 1204, Arlington, VA 22202-4302. Respondents should be aware that notwithstanding any other provision of law, no person shall be subject to any penalty for failing to comply with a collection of information if it does not display a currently valid OMB control number. **PLEASE DO NOT RETURN YOUR FORM TO THE ABOVE ADDRESS.**

1. REPORT DATE (DD-MM-YYYY) March 2006		2. REPORT TYPE Annual		3. DATES COVERED (From - To) 1 Mar 05 – 28 Feb 06	
Transurethral Ultrasound Diffraction Tomography				5a. CONTRACT NUMBER	
				5b. GRANT NUMBER W81XWH-04-1-0042	
				5c. PROGRAM ELEMENT NUMBER	
6. AUTHOR(S) Matthias C. Schabel, Ph.D.; Dilip Ghosh Roy, Ph.D. and Altaf Khan E-mail: mschabel@ucair.med.utah.edu				5d. PROJECT NUMBER	
				5e. TASK NUMBER	
				5f. WORK UNIT NUMBER	
7. PERFORMING ORGANIZATION NAME(S) AND ADDRESS(ES) University of Utah Salt Lake City, Utah 84112-9351				8. PERFORMING ORGANIZATION REPORT NUMBER	
9. SPONSORING / MONITORING AGENCY NAME(S) AND ADDRESS(ES) U.S. Army Medical Research and Materiel Command Fort Detrick, Maryland 21702-5012				10. SPONSOR/MONITOR'S ACRONYM(S) 11. SPONSOR/MONITOR'S REPORT NUMBER(S)	
12. DISTRIBUTION / AVAILABILITY STATEMENT Approved for Public Release; Distribution Unlimited					
14. ABSTRACT The potential for cost-effective tomographic imaging using ultrasound continues to be confronted with difficulties arising from the computational complexity of fully three dimensional object reconstruction in the diffraction regime. Development of fast and accurate forward and inverse models for ultrasound propagation in the biomedical frequency range of 1-10 MHz is essential for diffraction tomography to be a practical imaging modality. We have implemented a flexible, object-oriented simulation system in MATLAB for performing rapid two- and three-dimensional modeling of forward scattering using the conjugate gradient FFT method in conjunction with a fast linear adjoint approximation to the Jacobian. Nonlinear conjugate gradient inversion has been implemented and tested in both 2D and 3D, demonstrating the feasibility of the method for diffraction tomography. We have also implemented and tested several regularization schemes including L2-norm and total variation, and have used multigrid iteration in conjunction with anisotropic diffusion filtering to accelerate convergence of the inversion algorithm. Inversions of strongly scattering objects have been successfully performed in 2D and 3D, and results thereof are presented herein.				15. Subject Terms (keywords previously assigned to proposal abstract or terms which apply to this award) acoustic inverse scattering, acoustic tomography, Lippmann-Schwinger, Equation, conjugate gradient FFT, prostate imaging	
16. SECURITY CLASSIFICATION OF:					
a. REPORT U	b. ABSTRACT U	c. THIS PAGE U	18. NUMBER OF PAGES 27		
					19a. NAME OF RESPONSIBLE PERSON USAMRMC
			19b. TELEPHONE NUMBER (include area code)		

Contents

1	Introduction	2
2	Inversion in 2D and 3D	2
2.1	Inverse Modeling	2
2.2	Multigrid-Multifrequency Inversion	4
2.3	Inversion in the Exterior Source/Interior Detector Geometry .	5
2.4	Anisotropic Diffusion Filtering	6
2.5	Three-dimensional Reconstruction	6
3	Theoretical Developments	7
3.1	Scattering in the Interior-Interior Geometry	7
4	Simultaneous Reconstruction of Compressibility and Mass Density	9
5	Key Research Accomplishments	11
6	Reportable Outcomes	12
7	Conclusions and Future Work	12
7.1	Improving Forward Model Performance	13
7.2	The Inverse Problem	13
8	Figures	18

1 Introduction

The main objective of this project is the development of accurate physical models and efficient numerical algorithms suitable for diffraction tomographic reconstruction of the compressibility, acoustic attenuation, and mass density of the prostate through a multielement transurethral ultrasound transceiver. Unlike conventional ultrasound imaging, which is non-quantitative and affected by speckle artifacts, three-dimensional tomographic solution of the inverse acoustic scattering problem has the potential to quantitatively reconstruct the detailed acoustic properties of the prostate from measurements of the scattered radiation field. However, numerous challenges must be confronted before such a proposition becomes feasible in real-world applications. It is well-known that problems in inverse scattering, in addition to being mathematically complex and computationally intensive, are also particularly ill-posed and ill-conditioned.[1, 2, 3] This progress report takes up where our previous report, for the award period from March 1, 2004 through February 28, 2005, left off, so we minimize duplication of results already reported previously.

Our research over the past year has focused on three primary goals: 1) implementation and testing of various schemes for solving inverse scattering problems in 2D and 3D and their optimization; 2) development and testing of a theoretical foundation and practical implementation of the acoustic scattering problem in the endoluminal geometry in which the ultrasound transceivers are located within the lumen of the urethra (which we term *endoluminal ultrasound tomography*, ELUST), and 3) development of analytical and numerical contrast-source inversion procedures for simultaneous recovery of sound speed and mass density.[4, 5, 6, 7, 8, 9]

2 Inversion in 2D and 3D

2.1 Inverse Modeling

We have developed and implemented a nonlinear conjugate gradient (NLCG) algorithm [10, 11] for minimization of a two-term Tikhonov cost functional [3] incorporating both a χ^2 term for model-data agreement and a regularization term for object error. The advantage of NLCG algorithms over quasi-Newton methods is that they only require the evaluation of the gradient of the ob-

jective function, rather than its Hessian, potentially leading to significant computational and storage savings [10] in cases such as ours where function evaluations are expensive. We further improve the efficiency of our minimization scheme by implementing a gradient calculation based on the method of adjoint fields that allows us to forego the calculation of the full Jacobian matrix at each iteration. In our work to date we have considered both L_2 -norm and total variation based L_1 -functionals. The former tends to enforce a higher degree of smoothness on the solutions, while the latter is known to have better edge-preserving properties and is well suited to reconstruction of block objects with sharp boundaries. Both methods provide reasonably good results in the test phantoms we have considered, although total variation appears to be somewhat superior for the limited test cases studied so far. More work remains to be done to establish definitively if one is superior to the other for ELUST applications.

Care must be taken in the testing of the inversion algorithms to not commit an “inverse crime”. [1, 2] This happens when the same forward model is used to compute both “measured” and reconstructed scattered fields. In this case, it is possible to obtain spuriously good agreement of the reconstructed and true objects and be misled into overestimating the accuracy of the inversion scheme. For single or multifrequency reconstructions at a fixed grid size, we perform the following steps in computing the reconstructed object:

- **Calculate simulated measurement data from “true” object.** The “true” object is discretized on a finer grid than the highest resolution reconstruction desired (in our simulations, typically twice N_{recon}). For example, if we wish to reconstruct a phantom on a 64×64 grid, the measured scattered field is computed from an discretized phantom that is no smaller than 128×128 .
- **Add noise to measurement data:** Gaussian-distributed random noise with a standard deviation of $\simeq 2 - 3\%$ is separately added to the real and imaginary components of the measured scattered field.
- **Determine reconstructed object from inversion algorithm:** The cost functional is minimized using the NLCG routine to give the reconstructed object.

2.2 Multigrid-Multifrequency Inversion

A major impediment to the development of effective inverse scattering algorithms is the tendency of the solutions to become trapped in local minima of the objective function, leading to reconstructions that differ significantly from the true object and dependence on the starting guess. In order to combat this problem, we have developed a multigrid, multifrequency technique that appears to work quite effectively. In some cases, the effective regularization implicit in iteratively bootstrapping from low to high-resolution appears to obviate the need for a regularization term entirely. This technique is implemented as follows:

- **Choose the starting grid size for an initial, low-resolution reconstruction.** Typically, $N_0 \simeq 16$.
- **Choose a uniform object for the starting guess, γ_0 .** Typically, $\gamma_0 \simeq 0.01$.
- **k-th multigrid iteration:**
 - **Set wavelength for reconstruction:** Typically, $\lambda_k/L = 4/N_k$, where L is the physical dimension of the object, and λ_k , N_k are the wavelength and grid size, respectively, in the k-th iteration. Such a choice of λ_k and N_k allows the Nyquist sampling interval to be exceeded and thereby ensuring that the forward model is able to accurately represent the scattered field.
 - **Perform reconstruction:** γ_k is reconstructed by FFT-NLCG.
 - **Increment grid size:** $N_{k+1} = \beta N_k$. Typically, $\beta \simeq 1.25 - 2.00$.
 - **Compute an improved starting guess:** Upsample γ_k to resolution N_{k+1} to obtain γ_{k+1} .
- **Terminate iteration:** Finished when N_k reaches the ultimate desired size for the reconstruction.

In multigrid reconstructions, the measurement data for each resolution (and the corresponding frequency) is computed on the same grid size, normally twice the largest resolution to be reconstructed. This ensures that the inversion is not affected by discretization artifacts that change with lattice size. The effectiveness of the multigrid method is demonstrated in Fig. 1, where

we show the reconstructions of a Shepp-Logan phantom for a grid size of 128×128 using this approach. In this case, grid dimensions of 16, 20, 24, 28, 32, 40, 48, 56, 64, and 128 were used sequentially, and each reconstruction was computed using three wavelengths simultaneously: $\lambda = L$, $2L\sqrt{N}$, and $4L/N$. In the figure, panel (a) shows the true object at 256×256 grid resolution, and panel (b) shows the reconstructed object. It is apparent that we are able to resolve objects down to a size of approximately 4 pixels, as expected from the minimum wavelength used.

Multigrid inversion is compared with direct inversion without multiresolution bootstrapping in Figure 2. The upper panels (a-c) are reconstructions of the scatterer shown in Figure 3d performed without regularization ($\alpha = 0$) with a uniform starting guess for three different grid sizes and wavelengths defined by $\lambda/L = 4L/N$. Here, the Gibbs phenomenon is highly apparent, with the actual object ringed with large amplitude haloes. The lower panels (d-f) are identical except that multigrid iteration was utilized so that the starting guess for Figure 2e was an upsampled version of the reconstruction in Fig. 2d and the starting guess for 2f was an upsampled version of 3e. Here the regularizing effect of multigrid iteration is clearly apparent. The reconstructions in Figure 2a and Figure 2d are identical, but use of the lower frequency reconstructions as an initializer for the higher frequencies leads to dramatic improvement in the agreement between the true scatterer and the reconstructed objects.

2.3 Inversion in the Exterior Source/Interior Detector Geometry

In this geometry, the source is a plane wave, as previously, but the detectors are embedded in the object to be reconstructed. If it is assumed that the detectors are pointlike objects, and do not significantly perturb the scattered fields, then the forward problem can be treated in a manner similar to the conventional exterior source/exterior detector (or exterior-exterior) geometry. The main difference is that the scattered fields are now the same as the total internal fields.

In order to perform a feasibility test for reconstructing in an endoluminal geometry, we implemented a mixed geometry simulation in which plane wave sources are incident on the object from outside, but the detectors (which are regarded as pointlike and do not perturb the scatterer) are arrayed in

the interior of the object. As pointed out above, in the exterior/interior geometry, the internal fields are to be used for inversions rather than the scattered fields. We have considered both a standard modified Shepp-Logan phantom (Fig. 3a-c), and a phantom intended to more closely resemble a real endoluminal configuration (panels d-f). In both cases, we note that, although the effective maximum frequencies are relatively low ($\simeq 2$ MHz), the reconstructions clearly show the overall structure of the object and, in addition, reproduce many of the fine structures quite well.

2.4 Anisotropic Diffusion Filtering

As a consequence of the finite number of wavelengths used in reconstruction, images typically manifest a type of Gibbs ringing. Using multifrequency data for inversion, as in the reconstructions in Fig. 1, mitigates this significantly, though at the price of an increase in the computation time. The ringing is particularly apparent in panel (b) of the single frequency reconstruction of Fig. 3, where it is visible both within and outside the reconstructed object. A method for reducing noise in multidimensional data while simultaneously preserving sharp edges which has come into relatively wide use in image processing and computer vision in the past decade is known as anisotropic diffusion filtering (ADF) [12, 13]. Because we have a reasonable physical estimate of the length scale of these spurious oscillations, ADF is particularly easy to apply as a post-processing step once reconstruction is complete. The ability of ADF to remove the high-frequency noise without compromising the representation of the thin, strongly scattering shell is clearly demonstrated in panel (c) of Fig. 1 as well as panels (c) and (f) of Fig. 3. We have investigated the iteration properties of ADF of various reconstructions and find that, as shown in Figure 4, there is typically a minimum in the RMS error between the true and reconstructed objects for a finite number of ADF iterations in the range of 5-15. It appears that integration of a cycle of ADF into the multigrid reconstruction algorithm minimizes the appearance of spurious oscillations and leads to enhanced reconstruction accuracy, though future work is needed to establish the optimal parameter choices.

2.5 Three-dimensional Reconstruction

Figures 5-7 demonstrate the capability to perform full 3D reconstructions using the Lippmann-Schwinger forward model. In this case, the reconstruction

was performed in the exterior-exterior geometry, with 256 detectors arrayed in 4 rings of 64 lying perpendicular to the z-axis. While the computational demands limited the size of our reconstruction to $24 \times 24 \times 24$, so discretization and the relatively long wavelengths used make conditions sub-optimal for inversion, Figure ?? shows the ability to accurately depict the large scale interior structures of the object accurately, and appears to perform as well as the 2D algorithm at modeling the thin exterior shell. Other than reformulation of the scattering Green's function and use of three dimensional source and detector arrays, the 3D problem is handled by the same inversion code as 2D problems.

3 Theoretical Developments

3.1 Scattering in the Interior-Interior Geometry

The interior-interior scattering geometry is a novel geometry that is not conventionally considered in inverse scattering problems. In most cases, the source as well as detectors are exterior to the scatterer. In the endoluminal tomography (ELUST) of the prostate, sources and detectors are both internal to the organ. While our preliminary work will focus on extension of existing algorithms to the case of nonperturbing interior point sources, application of this methodology in an experimental setting will require treatment of the perturbation of the acoustic scattering caused by the presence of the catheter tip and transceiver array. We have developed a theoretical foundation for the case where it is assumed that the transducers are placed on the surface of a sound-impermeable cylinder located within the urethra. We treat this cylinder assuming Neumann boundary conditions where the normal component of wave velocity on the surface vanishes. In the usual, exterior-exterior geometry, the field propagator is the outgoing free-space Green's function, but the presence of the Neumann cylinder changes the situation in a complicated manner. The occurrence of multiple scattering not only in the tissue matrix alone, but between the tissue and the cylinder makes it necessary to modify the free-space Green's function. The resulting Neumann Green's function must obey the Helmholtz equation and satisfy both the Neumann boundary condition and Sommerfeld's radiation condition at infinity. For an arbitrary scatterer, such a Green's function is difficult to construct, but in

the canonical cylindrical geometry it is possible to obtain G_N :

$$G_N(x|y) = \frac{i}{4} \sum_{n=-\infty}^{\infty} e^{in(\phi-\phi')}. \quad (1)$$

$$H_n^{(1)}(k_0 r_{>}) \left[J_n(k_0 r_{<}) - \frac{J_n(k_0 a)}{H_n^{(1)}(k_0 a)} H_n^{(1)}(k_0 r_{<}) \right]$$

in 2-D, and

$$G_N(x|y) = \frac{i}{2} \sum_{n=-\infty}^{\infty} e^{in(\phi-\phi')} \quad (2)$$

$$\int_{R^1} dk_{\parallel} H_n^{(1)}(k_{\perp} r_{>}) \left[J'_n(k_{\perp} r_{<}) - H_n^{(1)}(k_{\perp} r_{<}) \frac{J'_n(k_{\perp} a)}{H_n^{(1)}(k_{\perp} a)} \right]$$

in 3-D. In Eq. (1), $x = (r, \phi)$, and $y = (r, \phi')$. Moreover, $r_{<(>)}$ implies the larger or smaller of r and r' . k_0 is the incident wavenumber, and J, H are the standard cylindrical Bessel and Hankel function, respectively [14]. In Eq. (2), $x = (r, \phi, z)$, $y = (r', \phi', z')$, $k_{\perp} = k_x^2 + k_y^2$, and $k_{\parallel} = \sqrt{k_0^2 - k_{\perp}^2}$. a is the radius of the cylinder. Cylindrical coordinates were used. The expression in Eq. (2) is for the *supersonic* waves only. For *subsonic waves*, where the waves are *evanescent*, the cylindrical Hankel functions must be replaced by the modified Bessel functions K_n [15].

The expression for the incident field resulting from an infinitesimal rectangular transducer on the cylinder surface has also been derived. We present only the 3-D result. Let the transducer be $2L$ long, located at a distance of Z from the origin of the cylindrical coordinate system on the cylinder, and have an angular width of $2\phi_0$. Moreover, let v_0, d_0, c_0, v_0 represent the amplitude of vibration of the transducer surface, the mass density, sound speed in the homogeneous ambient medium, respectively. Then the incident, $\psi(x)$, at a point $x = (r, \phi, z)$, was derived as:

$$\psi^{(in)}(x) = \frac{v_{0\perp} \phi_0 L}{\pi^2} (i d_0 c_0 k_0) \sum_{n=-\infty}^{\infty} e^{in\phi} \text{sinc}(n\phi_0) \cdot \int_{R^1} dk_{\parallel} \text{sinc}(k_{\parallel} L) \frac{G_n^{(1)}(k_{\perp} \rho)}{G_n^{(1)}(k_{\perp} a)} e^{ik_{\parallel}(z-(Z+L))}. \quad (3)$$

$\text{sinc}(x) = \sin x/x$, is the sinc-function. Now, for all practical purposes, both L and ϕ_0 are expected to be small. In that case, the sinc-functions can be approximated by unity, and Eq. (3) reduces to

$$\psi^{(in)}(x) = 2iv_{0\perp}\phi_0d_0c_0\frac{G_n^{(1)}(k_0\rho)}{G_n^{(1')}(k_0\perp a)}. \quad (4)$$

Note that the field given in Eq. (4) is roughly in the plane passing through the midplane of the transducer. This is interesting since it raises the possibility of doing 3-D imaging via reconstructing only 2-D planes, a much simpler proposition.

With G_N given in Eq. (2), and $\psi^{(in)}$ in Eq. (3) or Eq. (4), the scattered field anywhere in the prostate can be obtained by the *Lippmann-Schwinger integral equation of scattering*, which is:

$$\psi(x) = \psi^{(in)}(x) + \int_{\Omega} G_N(x|y)\gamma(y)\psi(y)dy. \quad (5)$$

4 Simultaneous Reconstruction of Compressibility and Mass Density

In ultrasonic medical diagnostics, essentially all attempts at quantitative acoustic imaging have focused on speed of sound and attenuation imaging,[17, 18, 19, 20] while neglecting mass density (ρ) variation. Addressing the latter is relatively more difficult than handling the compressibility (κ), because of the involved manner in which the density term appears in the basic integral equation of scattering. Unlike the compressibility, the density term involves differential operators, and consequently, simultaneous determination of compressibility and mass density from the scattering data is complicated.[16] This is the reason that the mass density reconstruction, when undertaken, is conventionally limited to the linearized Born-Rytov approximation or for uniform distributions.[21, 22, 23] We have developed a theoretical-numerical procedure for inverting both compressibility and density distributions under non-Born conditions.

The full scattering problem involving both (ρ) and (κ) is given by [24]:

$$(\Delta + k_0^2)p = -k_0^2\gamma_cp + \nabla \cdot (\gamma_\rho\nabla p) \quad (6)$$

plus Sommerfeld's *radiation condition*, namely

$$\lim_{|x| \rightarrow \infty} |x|^m [\partial_{|x|} p_s - ik_0 p_s i] = 0,$$

The corresponding integral equation of scattering is:

$$p_s = \int_{\Omega} G^{(0)}(x|y) [-k_0^2 \gamma_c p + \nabla \cdot (\gamma_{\rho} \nabla p)], \quad x \notin \Omega. \quad (7)$$

The free-space Green's function, $G^{(0)}$ is $(i/4)H_0^{(1)}(k_0|x-y|)$ in 2D and $[1/4\pi|x-y|]e^{ik_0|x-y|}$ in 3D. $\gamma_c = 1 - \kappa/\kappa_0$, and $\gamma_{\rho} = 1 - \rho_0/\rho$, are the deviations of κ and ρ relative to the background.

We have developed the equivalent source based recent method of *contrast-source inversion* (CSI). An earlier version of a CSI-like method was considered by Colton [1] in the context of obstacle scattering. The contrast-source inversion avoids solving the CPU-intensive full forward problem. Moreover, it employs only linear CG, in which the computationally most involved step length calculations can be performed analytically. In CSI, the objective functional is constructed as:

$$\Phi(\gamma_c, \gamma_{\rho}) = \frac{1}{2} \sum_{j=1}^J \left[\frac{\Phi_{Dj}}{\Phi_D} + \frac{\Phi_{Oj}}{\Phi_O} \right]. \quad (8)$$

The summation index j runs over the incident waves which are assumed to be J in number. Φ_{Dj} , and Φ_{Oj} represent the j -th least squares constraints on the data and the object error, respectively. Specifically, $\Phi_{Dj} = \|\Phi_D - G^{(0)} * \phi_j\|_D^2$, and the object residual is $\Phi_{Oj} = \|\mathcal{F}[p_j^{in} - G^{(0)} * \phi_j - \phi_j]t\|_C^2$. ϕ_j is the j -th equivalent source. C and D stand for the computational and the detector domain, respectively. The normalization constants in Eq. (8) are: $\Phi_D = \sum_{j=1}^J |\Phi_D|^2$ and $\Phi_O = \sum_{j=1}^J |\mathcal{F}p^{in}|^2$. \mathcal{F} is an operator given by: $\mathcal{F} = [-k_0^2 \gamma_c + \nabla(\gamma_{\rho} \nabla)]$. A comparison of \mathcal{F} so defined with its expression: $\mathcal{F} = -k_0^2 \gamma_c$ when only κ is to be reconstructed, demonstrates the complexity involved in inverting mass density. The iterative inversion proceeds by generating the sequences, $\{\phi_{jn}\}$, $\{\gamma_c\}_n$, and $\{\gamma_{\rho}\}_n$. Assume that $\{\phi_{j,n-1}\}$, $\{\gamma_c\}_{n-1}$, and $\{\gamma_{\rho}\}_{n-1}$ are known. The source, ϕ_j will be updated first after which the object parameters will be updated.

We have analytically calculated the key parameters needed for The CSI minimization of the functional in Eq. (8) requires analytical expressions for some key parameters. We have

- Developed the full analytic Fréchet derivative of Φ in $\phi_{j,n-1}$.
- Partially completed the analytic step lengths, α_n^ϕ , α_n^c , and α_n^ρ needed in updating the contrast and the source.
- We have also completed the modifications that are needed in (1) and (2) for complex compressibility, i.a., including attenuation.

The basic calculations for CSI inversion of (ρ) and (κ) will be complete shortly, and numerical implementation will be ready to be undertaken.

5 Key Research Accomplishments

The major accomplishments over the time period reported are inversions in 3-D and scattering and inverse scattering in the novel semi and fully endoluminal prostate scattering geometry. The key research accomplishments are itemized below.

- Numerical inversions in three dimensions.
 - Numerical implementation of 3-D Green’s function [25, 26].
 - Numerical implementation of CG-FFT [27, 28, 29] 3-D Lippmann-Schwinger forward solution using Richmond’s scheme of discretization [30].
 - Verifications of 3-D forward solutions against the analytical exact 3-D results.
 - Numerical NLCG 3-D inversion
- Initial investigation of various forms of regularizing functional and various approaches to optimizing the convergence of minimization of the objective function.
- Minimization of oscillatory reconstruction artifacts using anisotropic diffusion filtering.
- Numerical 2-D inversions in the novel exterior/interior semi-endoluminal prostate scattering geometry.

- Theoretical formulation of forward scattering in the novel fully endoluminal prostate scattering geometry.
- Development of theoretical and numerical procedures for simultaneous reconstructions of compressibility and density by the equivalent source based contrast-source inversion technique.

6 Reportable Outcomes

- Abstract and oral presentation at the 17th AnnualUCAIR Symposium, Park City UT, October 2005.
- Abstract presented at 2005 Fully Three-Dimensional Image Reconstruction Meeting in Radiology and Nuclear Medicine, Salt Lake City UT, July 2005.
- Invited talk on the application of the method of adjoint fields to inverse scattering at 2006 Acoustical Society of America Annual Convention, Providence RI, June 2006.
- Paper on the analysis of error propagation in nonlinear diffraction tomography to be submitted.

7 Conclusions and Future Work

From the discussions above, it is apparent that a sufficiently accurate representation of the prostate will require a resolution for which the computational burden will exceed reasonable limits for a single processor system. Fortunately, much of the CGFFT computation is readily parallelized to take advantage of multiprocessor hardware and/or high-performance computing cluster systems that are rapidly growing in popularity and availability. Nevertheless, while such approaches are likely to be relevant to this work, it still remains critical to investigate all avenues to improving the intrinsic algorithm performance before resorting to brute force. For the upcoming year, we will work in a number of areas:

7.1 Improving Forward Model Performance

- develop preconditioning strategies for acceleration of conjugate gradient convergence.
- implement the non-Uniform FFT [27, ?] to take advantage of unevenly spaced grids.
- predictor-corrector methods for minimizing evaluations of full forward model
- parallelization of forward model algorithm and testing on cluster system
- Further develop the theory and implement ELUST geometry for the prostate.
- Further develop theory, numerics and implement simultaneous inversion of complex compressibility and mass density.

7.2 The Inverse Problem

We have demonstrated the inversion efficacy of NLCG with the adjoint field gradient computation [31] by implementing it in the reconstructions of objects in both two and three dimensions. However, there is much improvement to be made in the inversion algorithm. Among the strategies which we intend to employ over the next year are:

- investigation of alternative and/or hybrid minimization strategies such as simulated annealing, genetic algorithms and CSI type techniques to be used in conjunction with nonlinear conjugate gradient methods to maximize convergence rate.
- investigate the effects of different regularizing functionals including total variation, maximum entropy, laplacian, and others, on the inverse problem convergence properties of inversion algorithms.
- parallelization of inversion algorithms.
- development of a realistic prostate phantom using MRI and conventional ultrasound data in conjunction with anatomic information.

- implementation and testing of 2.5D reconstruction using 3D forward modeling to compute the scattered field in conjunction with sequential planar 2D reconstructions of the scatterer.

References

- [1] D. Colton and R. Kress: *Inverse Acoustic and Electromagnetic Scattering Theory*, Springer-Verlag, 1992.
- [2] D.N. Ghosh Roy and L. Couchman: *Inverse Problems and Inverse Scattering of Plane Waves*, Academic Press, 2002.
- [3] P.C. Hansen: *Rank-deficient and Discrete Ill-posed problems*, SIAM, 1998.
- [4] R.E. Kleinman and P.M. van den Berg: A modified gradient method for two-dimensional problems in tomography, *J. Comput. Appl. Math.*, vol. 42, pp. 17-35, 1993.
- [5] P.M. van den Berg and R.E. Kleinman: A contrast source inversion method, *Inverse Problems*, v. 13, pp. 1607-1620, 1997.
- [6] P.M. van den Berg, A.L. van Broekhoven and A. Abubaker: Extended contrast source inversion, *Inverse Problems*, vol. 15, pp. 1325-1344, 1999.
- [7] N.N. Bojarsky: Inverse scattering inverse source theory, *J. Math. Phys.*, pp. 1647-1650, 1981.
- [8] A.J. Devaney, and G.C. Sherman: Nonuniqueness in inverse source and scattering problems, *IEEE Trans. Ant. Prop.*, vol. 30, pp. 1034-1037, 1982.
- [9] T.M. Habashy, E.Y. Chow, and D.G. Dudley: Profile inversion using the renormalized source type integral equation approach, *IEEE Trans. Ant. Prop.*, vol. 38, pp. 668-681, 1990.
- [10] J. Nocedal and S.J. Wright: *Numerical optimization*, Springer, New York, 1999.
- [11] D.G. Luenberger: *Linear and Nonlinear Programming*, Addison-Wesley, 1984.
- [12] L.I. Rudin and S. Osher: Total variation based image restoration with free local constraints, *Proc. IEEE, ICIUP94*, pp. 31-35, 1994.

- [13] L. Alvarez, F. Guichard, P.L. Lions and J.M. Morel: Axioms and fundamental equations of image processing, Arch. Rational Mech. Anal., vol. 123, pp. 199-257, 1993.
- [14] M. Abramowitz and I.A. Stegun: *Handbook of Mathematical Functions*, Dover, 1972.
- [15] E.G. Williams: *Fourier Acoustics*, Academic Press, 1999.
- [16] D. Mast: Empirical relationships between acoustic parameters in human soft tissue. Acoustics Res. Lett. Online, vol. 1, 37-42, 2000.
- [17] N. Duric, et al: Ultrasound imaging of breast tissue, Proc. SPIE Med. Imag., paper 5035-4, 2003.
- [18] N. Duric, P. Littrup et al: Development of ultrasound tomography for breast imaging: technical assessment, Med. Phys., vol. 32, pp. 1375-1386.
- [19] H. Zhao, Gu Xuejun and H. Jiang H, 2005: Model-based ultrasound tomography, Med. Phys., vol. 32, pp. 2659-2664.
- [20] K.J.W. Taylor et al: Ultrasound as a complement to mammography and breast examination to characterize breast masses, Ultras. Med. Biolo., vol. 28, 19-26, 2002.
- [21] S.J. Norton: Generation of separate density and compressibility images in tissue, Ultrasonic Imaging, vol. 5, pp. 240-252, 1983.
- [22] S. Mensah and J.P. Lafebvre: Enhanced compressibility tomography, IEEE trans. Ultras. Ferroel. Freq. Control, vol. 44, pp. 1245-1252, 1997.
- [23] R. Kower: Estimation of the density, the wave speed and the acoustic impedance function in ultrasound imaging, Inverse Problems, vol. 21, pp. 93-112, 2005.
- [24] P.M. Morse and K.U. Ingard: *Theoretical Acoustics*, Princeton University Press, 1968.
- [25] J. Wiskin: *Geometric and Integral Equation Methods for Scattering in Layered Media, Doctoral Dissertation, Department of Mathematics, University of Utah, Salt Lake City, 1991.*

- [26] D.T. Borup: *Fast-Fourier-transform based iteration methods for solving the electric field integral equation for anatomically detailed man models*, Ph.D. Thesis, Dept. of Electrical Engineering, University of Utah, Salt Lake City, 1989.
- [27] X.M. Xu and Q.H. Liu: Fast Spectral-Domain Method for Acoustic Scattering Problems, IEEE Trans. Ultrasonics, Ferroelectrics, and Frequency Control, vol. 48, pp. 522-529, 2001.
- [28] T.J. Peters and J.L. Volakis: Application of a conjugate gradient FFT method to scattering from thin planar material plates, IEEE Trans. Antenna Propag., vol. AP-36, pp. 518-526, 1988.
- [29] A.F. Peterson and R. Mittra: Method of conjugate gradient for the numerical solution of large-body electromagnetic scattering problems, J. Opt. Soc. Amer. A, vol. 2, pp. 971-977, 1985.
- [30] J.H. Richmond:, Scattering by a dielectric cylinder of arbitrary cross section shape, IEEE Trans. Antenna Propag., vol. AP-13, pp. 334-341, 1965.
- [31] S.J. Norton: Iterative inverse scattering algorithms: methods of computing Fréchet derivatives, J. Acoust. Soc. Am., vol. 106, 2653-2660, 1999.

8 Figures

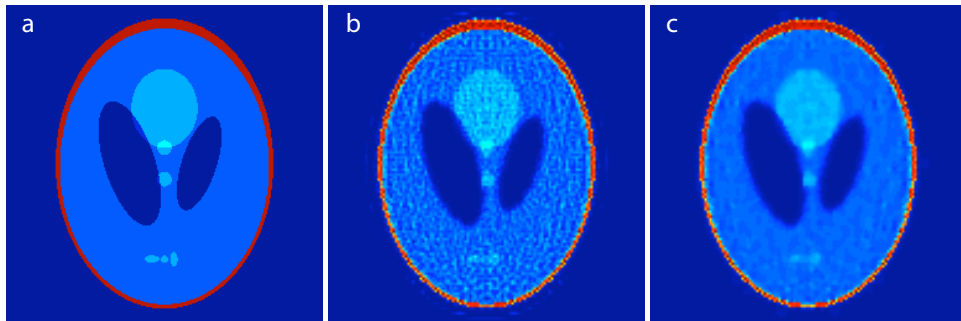


Figure 1: Reconstruction in the exterior geometry of a 2D scattering phantom on a 128×128 lattice. Panel (a) shows the true object, based on the modified Shepp-Logan phantom. Panel (b) shows the object reconstructed by our nonlinear conjugate gradient inversion algorithm with L^2 norm regularization, 24 incident plane waves with three wavelengths, and an array of 256 detectors located on a ring at a distance of $R_D = 4L$ from the center. Panel (c) shows the reconstruction from (b) with 8 iterations of anisotropic diffusion filtering applied to reduce Gibbs artifacts. The maximum scattering inhomogeneity of the object is $\gamma = 0.3$ and all three images are plotted on an identical intensity scale.

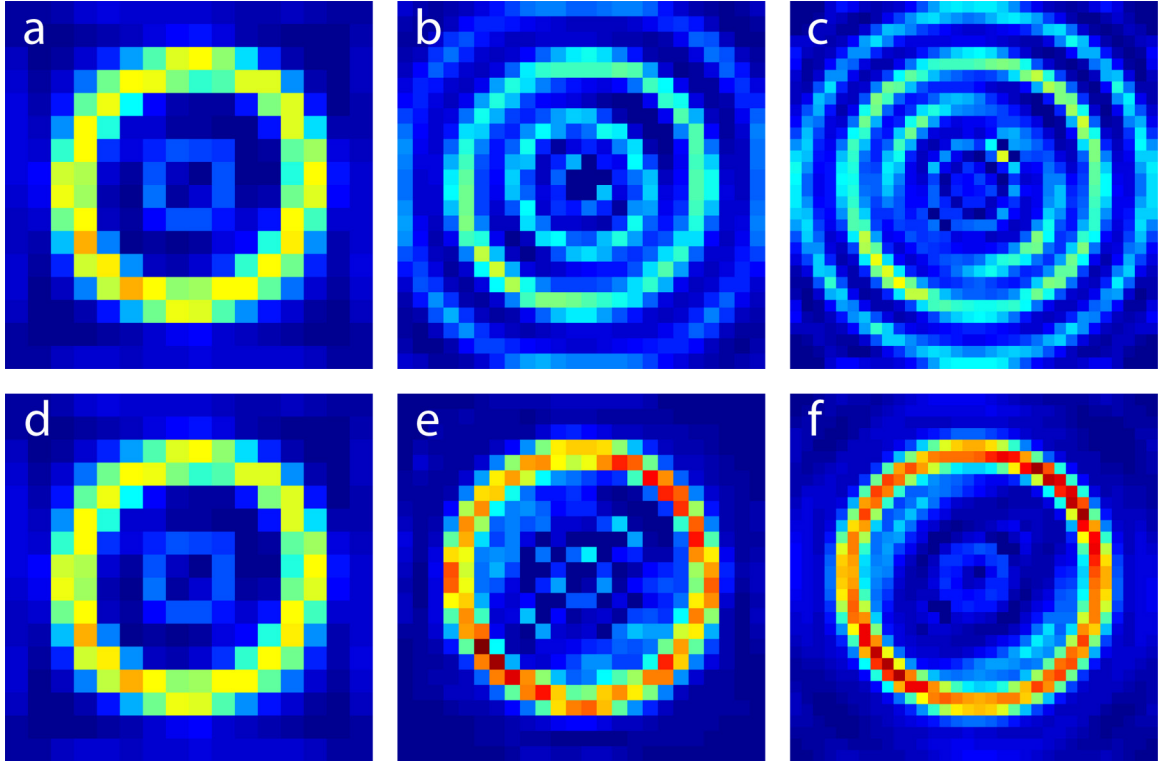


Figure 2: Comparison of reconstructions in the exterior/interior geometry without (panels a-c) and with (panels d-f) multigrid iteration, clearly demonstrating the regularizing effect of this approach. The true object, shown in panel (d) of Fig. 3, was discretized on a 128×128 grid. Reconstruction was performed with 64 incident waves and 64 detectors located as in the previous figure; the regularization parameter, α , was set to zero in both cases.

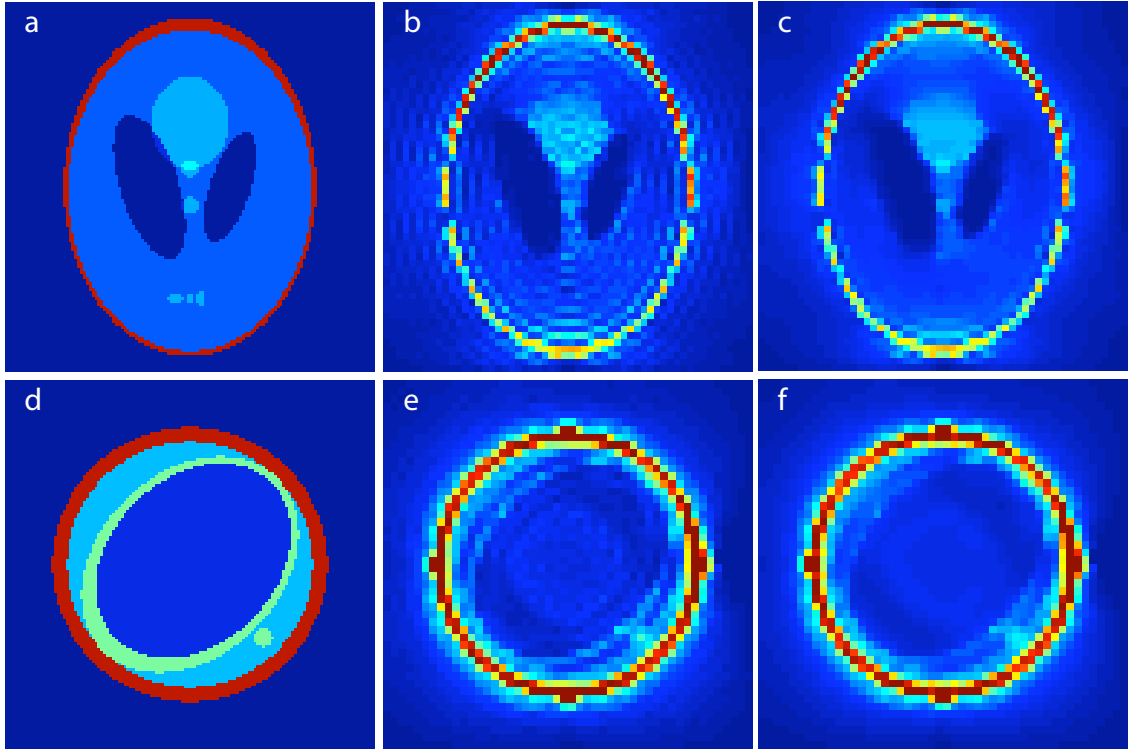


Figure 3: Reconstructions in the exterior/interior geometry. Panels (a-c) show the 56×56 phantom with $\gamma_{max} = 0.3$ (panel a), the multigrid reconstruction for 128 incident plane waves, and an array of 64 detectors located on a ring at a distance of $R_D = L/8$ from the center of the object (panel b), and the reconstruction from (panel b) after application of 5 iterations of anisotropic diffusion filtering to reduce Gibbs artifacts. Panels (d-e) show the same for a 48×48 phantom more representative of the endoluminal geometry. The reconstruction in panel (b) was performed with 64 incident plane waves and 64 detectors in the same configuration as panels (a-c). All objects are plotted on an identical intensity scale.

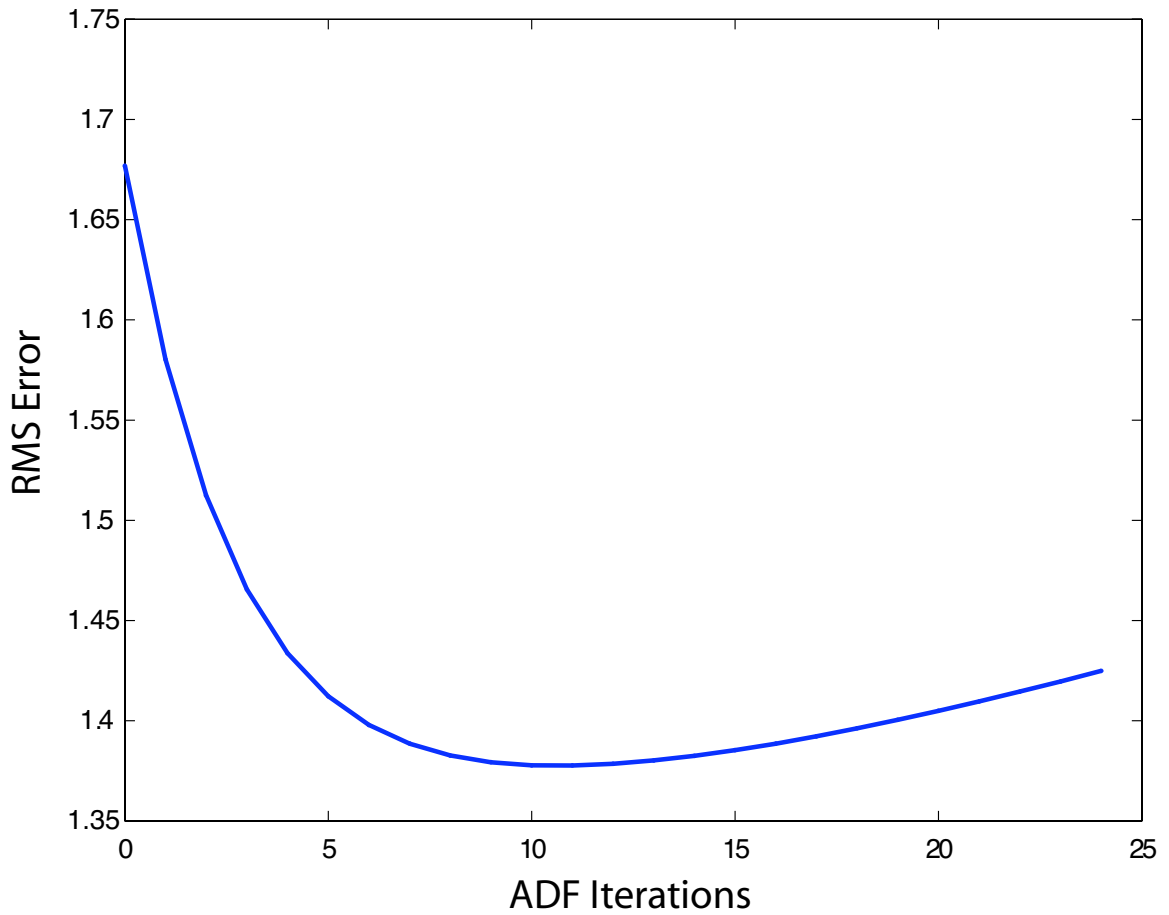


Figure 4: Residual root mean square (RMS) error between reconstructed and true object for the reconstruction shown in Figure 1 as a function of iterations of anisotropic diffusion filtering. The presence of a clear minimum for a finite number of iterations (in this case around 11) indicates that

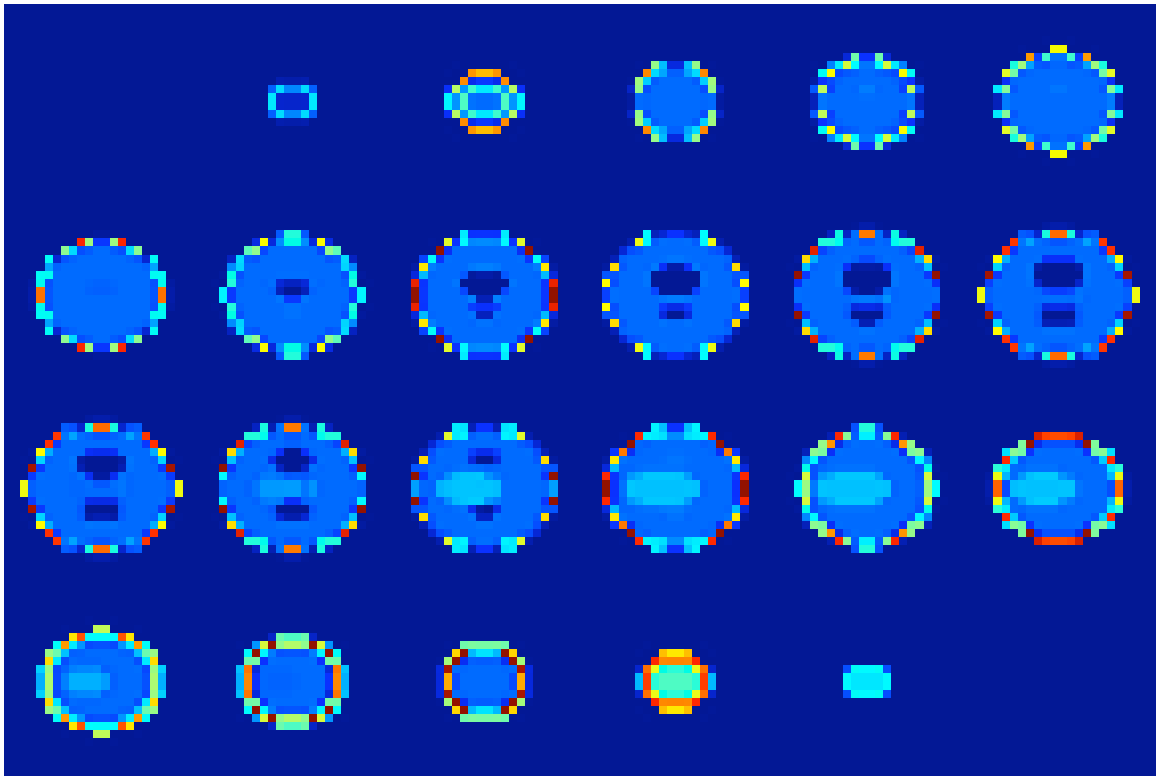


Figure 5: Sections through a $24 \times 24 \times 24$ numerical phantom developed as a 3D analog to the 2D acoustic Shepp-Logan phantom for testing three-dimensional reconstruction algorithms. Here, the maximum value of γ was 0.3.

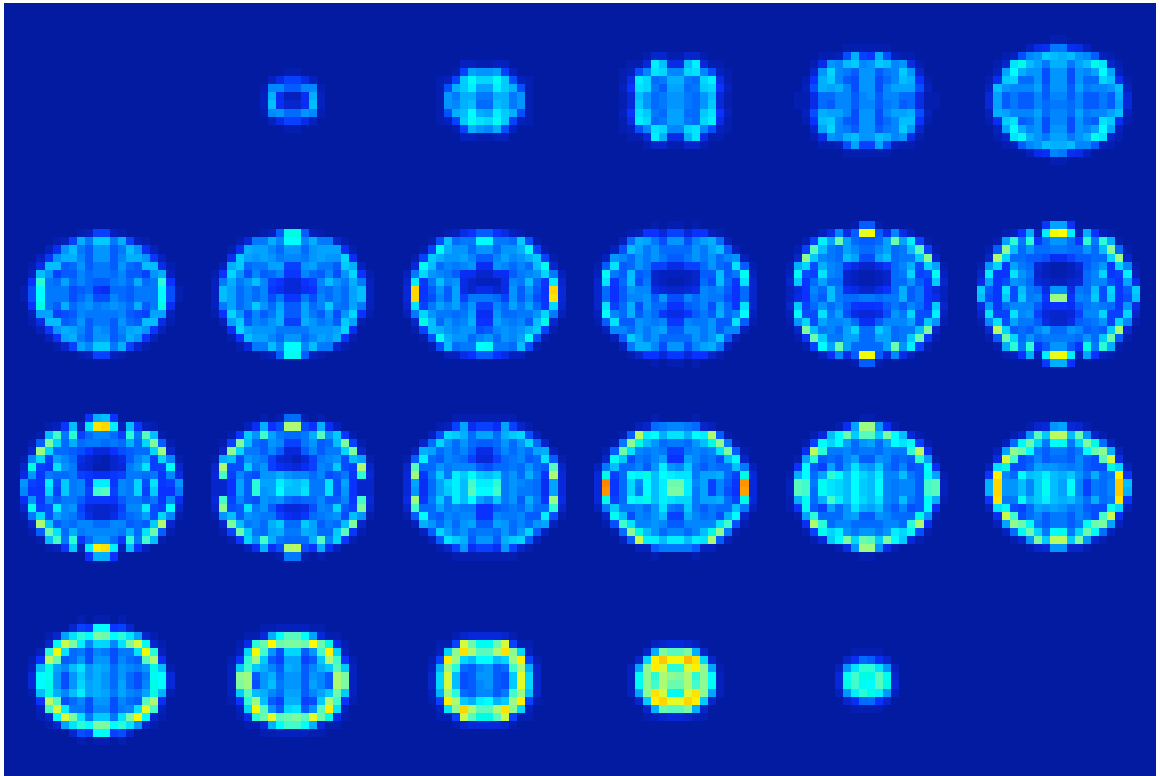


Figure 6: Sections of a multigrid reconstruction in 3D of the phantom shown in Figure 5. Here the total variation regularization term was used with $\alpha = 10^{-3}$. The scale is identical to that of Figure 5.

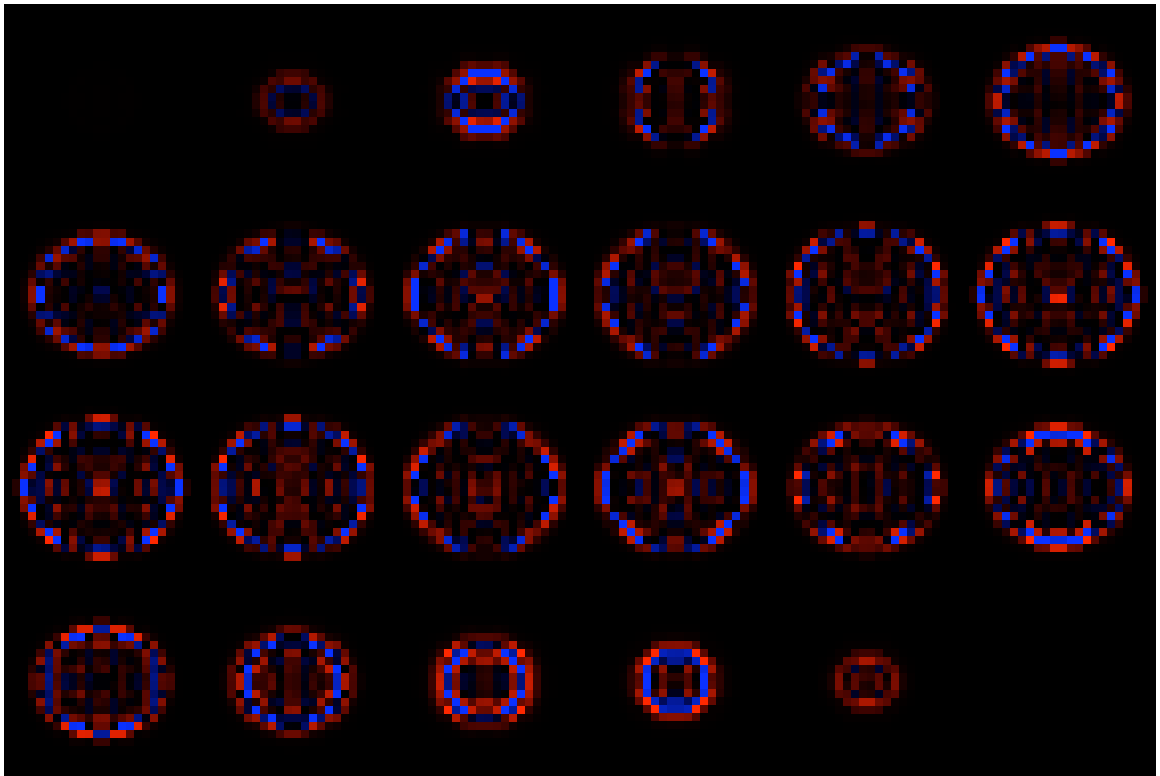


Figure 7: Reconstruction error for the 3D phantom plotted in Figure 5, plotted from -0.06 to 0.06.